# Underpinning Hybridization Intuition for Complex Nanoantennas by Magnetoelectric Quadrupolar Polarizability Retrieval

Felipe Bernal Arango, Toon Coenen, and A. Femius Koenderink*

Center for Nanophotonics, FOM Institute AMOLF, Science Park 104, 1098 XG Amsterdam, The Netherlands

**S** Supporting Information

**ABSTRACT:** A central idea in plasmonics and metamaterials is to interpret scattering resonances as resulting from hybridization of electric dipoles. Recent developments in metamaterials as well as in plasmonic Fano systems have further included magnetic dipoles and electric quadrupoles in this reasoning. We derive a method to retrieve dipole and quadrupole polarizability tensors of nano scatterers from full-wave simulations, which allows us to underpin this intuitive reasoning by quantifying the existent modes and their strengths in complex nano antennas. By application to a dolmen plasmon structure, we show how the retrieval sheds new light on plasmon induced transparency. Further, we show how to implement radiative corrections to a dipole—quadrupole model applicable when scatterers



are placed near a surface, sphere, or stratified medium, similar to the known correction of dipole polarizabilities by the local density of optical states. We demonstrate how this model allows us to interpret near field excitation data taken on plasmon antennas deposited on a high-index substrate.

**KEYWORDS:** plasmonic antennas, multipole polarizability, polarizability retrieval, hybridization, extended point dipole theory, backaction correction
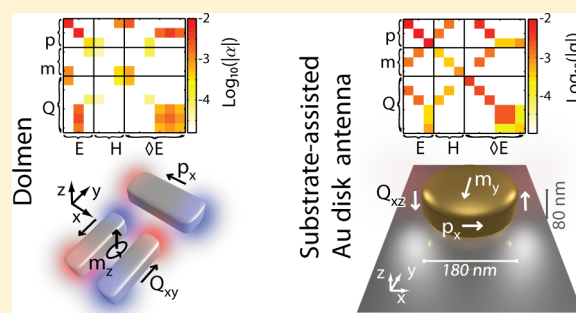
The fields of plasmonic antennas, metasurfaces, and metamaterials revolve around the idea that very strong scattering resonances in deeply subwavelength objects can be used to tailor the strength of optical near fields, scattering, and radiative processes.[1−3] Indeed, great strides have been reported in using engineered clusters of nanoparticles to enhance solar cell absorption,[4,5] LED light emission,[6,7] single molecule emission brightness and directivity,[3,8−13] optical sensing of very dilute analytes,[14−16] and the development of metasurfaces.[17,18] A workhorse interpretative tool to understand complex clusters of antennas is to reason in terms of coupled induced dipole moments that hybridize.[19−21] Surprisingly, once retardation and radiative corrections are taken into account, accurate results can be obtained for far-field observables such as extinction and scattering spectra, describing very well the essential physics of hallmark structures such as Yagi-Uda phased array antennas[10,11,22] as well as oligomers with plasmon induced transparency (PIT) features.[23−28] In fact, viewing a complex plasmon antenna as a collection of electric point dipoles has been employed not just as qualitative, but also as quantitative tool known as the "Discrete Dipole Approximation" (DDA) that is recognized to be valid as long as field gradients are small on the scale of the discretization.[29]

More recently, efforts in metasurfaces as well as in plasmonically induced transparency have underlined that, rather than separating a structure into a set of discrete constituent electric dipoles, intuition may be advantageously developed by assigning to a given structure not just an electric

dipole response, but also a magnetic dipole and electric quadrupole moment. While it is evident that both the DDA (taking many dipoles) and a full multipole expansion by definition can always capture the complete physics, the important notion here is that intuition benefits from reasoning with just a few terms, and that for moderately sized antennas the response is usually assumed to derive from at most three leading multipoles. The first is the electric dipole response to incident electric field that is key to plasmonic hybridization. The second is a resonant response to curls of the electric field that embody magnetism in metamaterials and is implicitly assumed whenever a metamaterial object is viewed as an LC resonator. The third is the resonant response of a structure to symmetric gradients of the electric field, that is, the electric quadrupole response. In recent works, this response has been invoked as responsible for the occurrence of sharp features in extinction of antennas such as dolmens.

Generally, when using the multipolar classification of modes for nano antennas, one fits optical responses of antennas to a coupled oscillator model, where one interprets the fitted coupling constants, damping rates, and resonance frequencies to represent properties of assumed quadrupole resonances (often coined "dark mode") electric and magnetic dipolar modes (often coined "bright"). We believe that rather than relying on intuition for attributing oscillators to multipole

modes, it would be desirable to have a quantitative method to establish whether the intuition is correct that magnetic dipoles, electric dipoles, and electric quadrupoles are at play, with which amplitude ratio and phase they are excited, and how they each contribute in terms of scattering strength, resonance frequency, and width. One should realize that the common underpinning of intuition by examination of snapshots of field or charge distributions from full-wave simulations at distinct frequencies is problematic, since snapshots represent unseparated superpositions of excited modes. For particular structures, several authors have sought to overcome this problem.[28,30] Here we propose a method to retrieve and visualize electric and magnetic dipolar polarizabilities as well as quadrupolar polarizabilities, that generically allows us to underpin the intuition of what modes are involved in the scattering processes. As a useful byproduct this model can be used not just as an a posteriori interpretative tool. In a predictive manner, the output of our polarizability retrieval can be used as input for self-consistent multiple scattering calculations[20,21,31] for point particles to which the retrieved responses are assigned. This predictive power allows us first to design new structures, and second to put the intuitive reasoning to the test and find out until what point it remains valid.

## RETRIEVAL OF QUADRUPOLES AND REDUCTION OF TERMS

The starting point of our work is chapter 9 in the book of Jackson[32] and recent work by Mühlig et al.[33] To recapitulate this starting point, we assume that a full-wave solution for the near field of the scatterer of interest in a homogeneous medium upon plane wave excitation is available. While any method may be used, we employ a surface integral equation method (SIE)[34] that we implemented previously.[35] To derive induced multipole moments, we use the fact that the vector spherical harmonic functions $\mathbf{N}_{nm}(r,\theta,\phi)$ and $\mathbf{M}_{nm}(r,\theta,\phi)$ form a complete and orthonormal set.[36] Therefore, the scattered near field $\mathbf{E}(r,\theta,\phi)$ has a unique expansion

$$\mathbf{E}(r,\theta,\phi) = \sum_{n=1}^{\infty} \sum_{m=-n}^{n} [a_{nm}\mathbf{N}_{nm}(r,\theta,\phi) + b_{nm}\mathbf{M}_{nm}(r,\theta,\phi)]$$

(1)

where the expansion coefficients $a_{nm}$ and $b_{nm}$ can be simply found by projecting the calculated $\mathbf{E}(r,\theta,\phi)$ on the vector spherical harmonic functions. The expansion coefficients are linearly related to the multipole moments. As explained by Bernal Arango et al.,[35] one can very efficiently calculate the coefficients with excellent accuracy using numerical integration on just very few sampling points with points and weights chosen consistent with Legendre quadratures,[37] owing to special properties for discrete Fourier transforms on the unit sphere.

Having summarized the established starting point, we turn to the key question, that is, how to reconstruct and analyze polarizabilities given that it is possible to calculate multipole moments for any illumination condition. The polarizability is the central quantity that summarizes the possible responses of a scattering unit to arbitrary incident fields, and can be used as input for predictive modeling of complicated arrangements of such units. For electric and magnetic dipoles, deriving the polarizability from calculations of induced moments is completely resolved in ref 35. Therefore, the key ingredient

in this work is to revisit the quadrupole tensor. The quadrupole moment is defined as a symmetric traceless tensor.[32]

$$\bar{\mathbf{Q}} = \begin{pmatrix} Q_{xx} & Q_{xy} & Q_{xz} \\ Q_{xy} & Q_{yy} & Q_{yz} \\ Q_{xz} & Q_{yz} & Q_{zz} \end{pmatrix}$$

(2)

In a deeply subwavelength object the quadrupole moments are generally set up by the symmetric part of the gradients of an incident electric field through a fourth rank "quadrupolarizability"[38] tensor[39,40] $\alpha_{ijmn}^{Q}$

$$Q_{ij} = \alpha_{ijmn}^{Q}(\partial_m E_n + \partial_n E_m)/2$$

(3)

Here we use the Einstein summation notation and abbreviate the spatial derivatives $\partial/\partial_{x_m}$ as $\partial_m$ ($m = 1, 2, 3$ for $x,y,z$). If we use the fact that both the traceless tensor $Q_{ij}$ and the tensor $(\partial_m E_n + \partial_n E_m)/2$ are symmetric, we can eliminate some redundancy in eq 3 and obtain a much simpler matrix equation $Q_i = \alpha_{ij}^{Q} \Diamond E_j$. Here, the vectors

$$\mathbf{Q} = \{2Q_{xy}, 2Q_{xz}, 2Q_{yz}, Q_{xx}, Q_{yy}, Q_{zz}\}$$

(4)

and

$$\Diamond\mathbf{E} = \{(\partial_x E_y + \partial_y E_x)/2, (\partial_x E_z + \partial_z E_x)/2,$$
$$(\partial_y E_z + \partial_z E_y)/2, \partial_x E_x, \partial_y E_y, \partial_z E_z\}$$

(5)

represent complete information on the quadrupolarizability tensor and the Diamond operator $\Diamond$ is introduced to ease the handling of the symmetric gradient operations.

We now combine this insight for quadrupoles with the insight we reported in refs 31 and 35 for electric and magnetic dipole polarizability. We define the combination of dipole and quadrupole response as a "superpolarizability" $\bar{\alpha}^S$ tensor of the form:

$$\begin{pmatrix} \mathbf{p} \\ \mathbf{m} \\ \mathbf{Q} \end{pmatrix} = \bar{\alpha}^S \begin{pmatrix} \mathbf{E} \\ \mathbf{H} \\ \Diamond\mathbf{E} \end{pmatrix}$$

(6)

An important practical merit of this definition over the use of the rank 4 quadrupolarizability tensor is that the rank 2 superpolarizability tensor can be immediately plotted as a 2D color image, allowing direct comparison of dipolar and quadrupolar contributions. The superpolarizability furthermore leaves open the possibility that a scatterer or scattering cluster is strongly plasmonic (electric dipole polarizability is dominant), a metamaterial object (magnetic dipole polarizability is strong), bianisotropic (cross-polarizability in which magnetic (electric) driving begets an electric (magnetic) dipolar response, as in an LC-resonator), and quadrupolar. The quadrupole could be driven by the six components of $\Diamond\mathbf{E}$, as appropriate for a deeply subwavelength object, or by $\mathbf{E}$ or $\mathbf{H}$ through an equivalent of "bi-anisotropic cross-coupling", as we will see below for the well-known dolmen plasmon antenna.

To find the $12 \times 12$ superpolarizability of an arbitrarily shaped object it is necessary to supply sufficient linearly independent incident conditions, retrieve the induced moments, and then perform matrix inversion. A subtle point is that invertibility requires to remove one more degree of redundancy, which owes to the facts that the quadrupole

tensor is traceless $Q_{xx} + Q_{yy} + Q_{zz}$, and that $\mathbf{E}$ is divergence free, that is, $\partial_x E_x + \partial_y E_y + \partial_z E_z = 0$. Throughout this work we plot the full $12 \times 12$ superpolarizability, while for calculations that require matrix inversion we cast to and from the equivalent $11 \times 11$ form as listed in the Methods section. A sketch of the 11 required driving conditions is presented in Figure 1. First, to
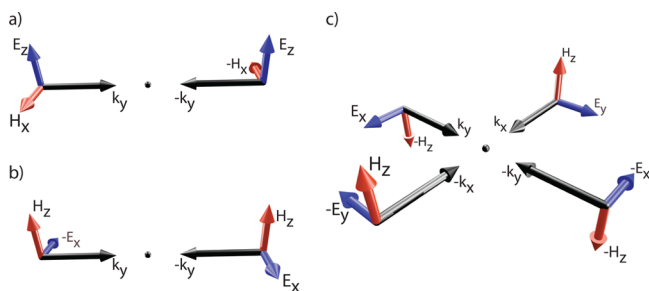


**Figure 1.** Sketches of the plane waves we combine to obtain linearly independent driving for retrieving superpolarizability tensors. (a) A pure electric field $\mathbf{E}$ at the origin is obtained from counterpropagating plane waves. (b) The same plane waves, but shifted in phase provide $\mathbf{H}$ at the origin, with a null in $\mathbf{E}$. As shown in (c), a combination of four plane waves in a plane can be combined to obtain a pure "symmetric gradient" in $\mathbf{E}$ without admixture of asymmetric gradient terms. It should be noted that the condition in (b) is not pure in the sense that it contains not only $\mathbf{H}$ but also a contribution from $\diamondsuit \mathbf{E}$.

construct three incidence conditions that only provide an electric field at the origin, without any magnetic field or electric-field gradient, we take counterpropagating copolarized plane waves along the three Cartesian axes. Figure 1a shows such a driving for the $y$ axis. Next, to provide no electric field but a magnetic field at the origin, we shift the three standing waves by $\lambda/4$. Figure 1b also shows such a driving for the $y$ axes. It should be noted that this condition is not, in fact, free of electric field gradient at the origin. To form the five required electric field gradients without any admixing of $\mathbf{E}$ and $\mathbf{H}$ we use two orthogonal pair sets of counterpropagating plane waves with antiparallel polarization of the $\mathbf{E}$ field. Figure 1c shows the combination of these four plane waves in the $xy$ plane, which generates the required $\diamondsuit E_{xy}$ driving. We create three of the five required excitations with zero $\mathbf{E}$ and $\mathbf{H}$ field, but a strong field gradient at the origin by combinations along the Cartesian axes. In addition, two excitations are created by using diagonals of the Cartesian cube. The superpolarizability simply follows from matrix inversion and is in fact entirely independent of the actual choice of linearly independent input fields. Finally we note two important facts. First it is important to realize that the simplification to a superpolarizability tensor does *not* involve an electrostatic approximation. Indeed, we use vector spherical harmonic projection of the full field solution to obtain the generalized Mie coefficients $a_{nm}$ and $b_{nm}$, that is, the electrodynamic multipole coefficients that include all retardation effects. Second, while it is the sole purpose of this paper to derive an interpretative tool to underpin prior works that have invoked electric dipole, magnetic dipole, and electric quadrupole responses only, the method can be extended also to include higher order moments. In particular, we note that while so far it has often been taken at face value that orders beyond the electric quadrupole are not relevant, the important question whether taking only the selected multipole terms indeed suffices at all is easily answered for any structure simply by

calculating the higher order expansion coefficients of the scattered field using eq 1.

**Dolmen $\alpha^S$-Tensor.** To demonstrate the utility of the multipole polarizability retrieval for the rigorous underpinning of hybridization intuition, we apply it to retrieve the $\alpha^S$-tensor of a silver dolmen structure. This structure is composed of a single $x$-oriented rod closely coupled to a $y$-oriented dimer of rods and is well-known because it exhibits PIT[24,26,30,41−44] when measuring extinction for $x$-polarized light incident along $z$. The structure used in our calculations is shown in Figure 2a
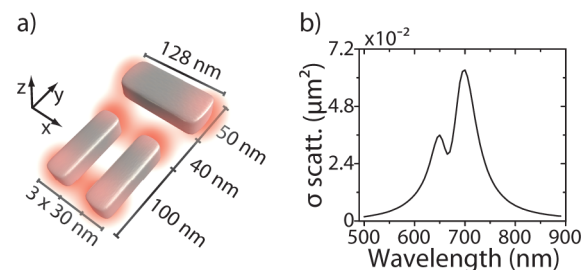


**Figure 2.** (a) Sketch of the dolmen structure with the dimensions used. (b) Total scattering cross section of the silver dolmen structure. The thickness is 20 nm.

with the corresponding dimensions. For the silver material, we use the tabulated data in ref 45. In Figure 2b we show the total scattering cross section of the structure as a function of optical wavelength. The resonant scattering cross section has two distinct features. The dominant feature is a maximum cross section at 687 nm, with a minimum close by at 665 nm. The spectral features are in good agreement with literature reports.[41] The proposed physics in those reports is that a Fano resonance occurs upon direct driving of the $x$-oriented dipolar resonance, which in turn through near field coupling drives a dark quadrupolar resonance of the dimer.[41]

We retrieve the $12 \times 12$ superpolarizability of the entire dolmen and visualize its elements in Figure 3a. Figure 3a shows $\alpha^S$ at a wavelength of 665 nm as a color plot, where we present the logarithm of the magnitude of the elements of $\alpha^S$. The logarithmic scale has the merit that it allows us to quickly
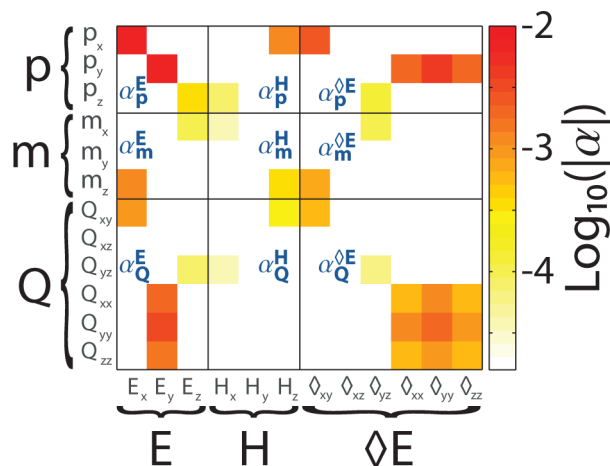


**Figure 3.** Graphical representation of the dolmen superpolarizability at the Fano resonance, that is, at $\lambda = 665$ nm. The color scale maps the logarithm $\log_{10}(|\alpha^S|)$, where $\alpha^S$ is expressed in units of $\mu m^3$ (see Methods).

identify the entries that dominate the optical response as the red/orange color (see Methods). Since the logarithmic scale unfortunately obscures small relative differences between elements (differences smaller than a factor 2) as well as phase information, we also report quantitative values for all non-negligible tensor elements in the Supporting Information, and plot the amplitude and phase for select elements in Figure 4. While all the equations in the main body of this paper are
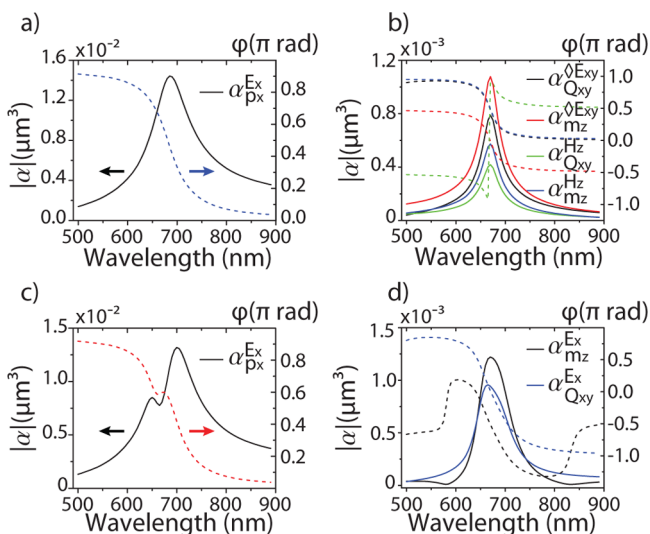


**Figure 4.** Magnitude and phase as a function of wavelength of salient superpolarizability tensor elements for (a) the isolated dolmen constituent top rod, (b) the isolated $y$-oriented dimer, and (c, d) the full dolmen. (a, c) Electric dipole polarizability along $x$. (b, d) Degree to which the magnetic dipole $m_z$ and electric quadrupole $Q_{xy}$ can be driven, which are intrinsic to the dimer asymmetric mode. For the isolated dimer, their driving requires $H_z$ or $\Diamond E_{xy}$ (b), while in the dolmen, the coupling to the top rod allows driving through $E_x$.

stated in SI units, for visualization it is convenient to scale the entries on the basis of a CGS-based unit system explained in the Methods section that ensures that all superpolarizability tensor elements have units of volume, with numerically equal entries (i.e., identical color in Figure 3a) corresponding to equal scattering power.

To understand the structure of the reported tensor, the $\alpha^S$ tensor can be divided in nine block matrices: four $3 \times 3$ matrices, two $3 \times 6$ matrices, two $6 \times 3$ matrices, and one $6 \times 6$ matrix. Throughout its diagonal we find that the first block matrix ($\alpha_p^E$) is related to the purely electric dipolar response of the object, meaning that it quantifies the electric dipole created by an electric field. For the dolmen structure at 665 nm, one finds a strong electric dipole polarizability $\alpha_{p_x}^{E_x} = 7.8 \times 10^{-3}\ \mu m^3$ along $x$, attributable to the resonance of the top rod. The two $y$-oriented rods are responsible for a sizable electric dipole polarizability $\alpha_{p_y}^{E_y} = 7 \times 10^{-3}\ \mu m^3$ along $y$. While their resonance is shifted away from that of the $x$-oriented rod toward the blue to 625 nm, their large joint volume still ensures a significant polarizability comparable to that of the single $x$-rod. Finally, due to the small height of the rods, the electric dipole polarizability along $z$ is only $\alpha_{p_z}^{E_z} = 3.4 \times 10^{-4}\ \mu m^3$.

The second diagonal block ($\alpha_m^H$) of the $\alpha^S$ tensor can be likewise interpreted as the purely magnetic dipolar response due to incident magnetic fields, while the third diagonal block is the quadrupolar response of the object due to symmetric

gradients of the electric field ($\alpha_Q^{\Diamond E}$), also called "quadrupolarizability" tensor.[39] The blocks outside the diagonal quantify cross-coupling terms. In particular, the $3 \times 3$ off-diagonal blocks quantify bianisotropy, that is, the generation of a magnetic dipole response upon driving by electric fields ($\alpha_m^E$) and vice versa. Finally, we also find quadrupoles induced directly by an electric or magnetic field ($\alpha_Q^E\ \alpha_Q^H$), which we define here as "hyperpolarizability" tensors. In terms of polarizability contributions that stand out for the dolmen in terms of magnitude (apart from the electric dipole polarizability), we find that a strong $z$-oriented magnetic dipole as well as a strong $Q_{xy}$ can be induced by driving simply with an $x$-oriented **E**-field (first column of $\alpha^S$, discussed at length below), while driving by $y$-oriented **E**-fields (second column) sets up a strong linear quadrupole moment along $y$ (since $Q_{yy} = -2Q_{xx} = -2Q_{zz}$ [phase not shown in plot], with all other quadrupole moments negligible). We further note the approximate symmetry of $\alpha^S$, which for purely dipolar magnetoelectric scatterers (top $6 \times 6$ block) is rigorous and a consequence of Onsager reciprocity.[31,46]

Evidently, the entire $\alpha^S$ tensor contains very rich physics that will allow one to pinpoint for each excitation condition exactly which moments are induced. Such insights may then be further cast into a microscopic analysis by examining how particular incident field distributions set up, for instance, particular charge oscillations inside the cluster. To illustrate how such an analysis can enrich insights in important optical phenomena, we focus on the dolmen response to an $x$-polarized plane wave, that is, the first column of $\alpha^S$ only. The retrieved polarizability shows that the dominant responses driven by an $x$-polarized plane wave as used in all reported experiments involve $p_x$ and the expected "dark" quadrupole $Q_{xy}$. More unexpectedly, an out-of-plane magnetic response $m_z$ also is significant. These three response contributions are cross coupled in the sense that driving any of the three "directly" via the diagonal of $\alpha^S$ also excites the others. For instance, in the original description of PIT experiments it is understood that one drives $p_x$ directly by $E_x$, which then induces the expected in-plane quadrupole response $Q_{xy}$ (as well as the associated magnetic response $m_z$). Conversely, the quadrupole can also be directly driven via application of the symmetric **E**-field gradient $\Diamond E_{xy}$, in which case also an electric dipole moment $p_x$ is induced. Thus, the polarizability tensor directly evidences the suspected hybridization of an $x$-oriented electric dipole with the $Q_{xy}$ dipole moment. Furthermore, our results point at an accompanying magnetic response that was not invoked in previously reported discussions on PIT in dolmens.

In regard to the microscopic analysis of their origin, out of these three contributions, the $p_x$ and $Q_{xy}$ were already assigned in literature to the fundamental dipole mode of the top rod and the antisymmetrically oscillating dimer, respectively. This assignment can be further underpinned by examining separately the superpolarizabilities of the isolated particles that compose the dolmen, that is, the $x$-oriented rod on one hand and the dimer on the other hand. As shown in Figure 4a, the isolated top particle has a strong electric dipole polarizability $\alpha_{p_x}^{E_x} = 14.4 \times 10^{-3}\ \mu m^3$ that is resonant at 687 nm with a width of 89 nm. The top particle alone is responsible for essentially the complete response of the $x$-oriented electric polarizability of the entire dolmen. The isolated dimer in contrast (Figure 4b) shows a resonance that carries both the expected quadrupolar $\alpha_{Q_{xy}}^{\Diamond E_{xy}}$ that PIT literature has focused on, and the magnetic

dipole $\alpha_{m_z}^{H_z}$ that was hitherto disregarded in PIT literature but emphasized in literature on metamaterial applications for cut wire pairs.[47] These moments are associated with the same asymmetric current distribution mode of the bare dimer, centered at 665 nm, with a width of 50 nm. Clearly, the magnetic dipole and electric quadrupole belong to the same resonance and share cross polarizabilities. This feature is generally found for antennas constructed by two separated electric dipoles, such as in cut-wire pairs.[47,48] Meyrath et al.[49] in a critical appraisal of the law of electromagnetic induction have argued that in the absence of closed conduction loops and given the nonelectrostatic nature of the system, a strict separation can not be made between magnetic and electric responses. We note that the induced moments can, through eq 1, be clearly separated, either mathematically on the basis of projection on vector spherical harmonics or in an experimental observable such as the far-field angular radiation pattern that differs markedly for magnetic dipoles and electric quadrupoles.[50] The ambiguity that Meyrath et al.[49] point out, however, is evident in the fact that the asymmetric resonance can not be uniquely assigned either to a response to magnetic field $H_z$ or to a response to nonuniformities in electric field. Indeed, the asymmetric mode of the cut-wire pair is simply driven by $\partial_x E_y$, which is contained equally in the curl of E (i.e., in $H_z = \partial_x E_y - \partial_y E_x$) and in the symmetric gradient (i.e., in $\diamondsuit E_{xy} = 1/2[\partial_x E_y + \partial_y E_x]$).

Returning to the superpolarizability for the entire dimer, we consider the frequency dependence of select components in Figure 4c to trace the emergence of PIT. For $\alpha_{p_x}^{E_x}$ the dipolar polarizability of the rod gains a dispersive Fano resonance at 665 nm, demonstrating that hybridization occurs. As complementary information, Figure 4d demonstrates that the resonances of the strong cross polarizabilities $\alpha_{m_z}^{E_x}$ and $\alpha_{Q_{xy}}^{E_x}$ likewise are a product of the hybridization of the composing elements, where the quadrupole contribution broadens as a consequence of coupling to the bright dipolar resonance of the rod. Thus, the simple superpolarizability retrieval presented here provides important underpinning for the physical picture proposed in literature. Rather than resorting to quasi-electrostatics or visually inspecting snapshots of simulated charge distributions, the superpolarizability tensor quantitatively reports which multipole moments are involved.

As a further insight that is provided by the superpolarizability analysis, we find that it allows us to quantify the common assumption that the dimer resonance with its combined electric quadrupole and magnetic dipole moment is a *dark* resonance. As we see from the plotted amplitudes of $\alpha^S$, the magnetic and quadrupolar moments induced through the incident electric field scatter comparable amounts, and the total power radiated by the asymmetric mode is within a factor 3 from that radiated by the induced electric dipole. To summarize, while the term "dark" adequately describes the lack of direct coupling between an incident x-polarized plane wave incident along z and the asymmetric mode, the radiation pattern of a dolmen actually contains significant contribution from the asymmetric mode in apparent contradiction to the terminology "dark" resonance.

A third observation is that the Fano line shape is ultimately determined not only by the amplitude, but also by the phase of the cross-polarizability, as motivated from a coupled oscillator model by Zhang et al.[41] In principle, the superpolarizability tensor provides a direct method to read off and microscopically understand the phase. Finally, we note that as in any optical

Fano system, a challenge is to ultimately identify the true normal, that is, *uncoupled* eigenmodes, as was recently reported for the Fano resonance in plasmonic heptamers[28] and investigated by Gallinet et al.[30] We propose that such an analysis can be realized by examining poles of the super-polarizability as one sweeps frequency into the complex frequency plane.[20,51,52]

## BACKACTION CORRECTION FOR HYBRIDIZATION WITH ENVIRONMENTS

In nano-optics one frequently relies on first developing intuition for the functioning of antennas or Fano-resonant structures when they are in isolation, to then explore the functioning of these structures in more complex geometries. Examples are the placement of antennas in arrays or the placement of antennas on dielectric interfaces or stratified media. For instance, plasmon antennas are used on dielectric interfaces such as glass coverslips in microscopy experiments[8,9,11,53] and sensing applications or on high-index semiconductors in LEDs and solar cell applications.[4,5] Here we ask if an extracted superpolarizability for a complex antenna in isolation can be used as input for a predictive model where the antenna is placed in a complicated environment. In the dipole approximation, the environment can be taken into account in the electric dipole polarizability by including radiation damping and a reactive shift in the polarizability as a self-interaction term that is essentially the scattered Green function of the embedding medium.[22,28,54,55] This correction is of large use, since with this correction it is possible to quantitatively predict the response of arbitrary antenna geometries in complex backgrounds using as input single building blocks for which the free space superpolarizability is already tabulated. Here we derive a similar correction for the superpolarizability. In

$$\begin{pmatrix} \mathbf{p} \\ \mathbf{m} \\ \mathbf{Q} \end{pmatrix} = \bar{\alpha}^S \begin{pmatrix} \mathbf{E} \\ \mathbf{H} \\ \diamondsuit \mathbf{E} \end{pmatrix} \qquad (7)$$

one should take into account that the driving field $(\mathbf{E}, \mathbf{H}, \diamondsuit\mathbf{E})$ should not just be the incident field, but also the field that comes back via interaction with the background to the scatterer, as quantified by the scattered part of the Green's function of the background system. Thus, the *total* field reads

$$\begin{pmatrix} \mathbf{E} \\ \mathbf{H} \\ \diamondsuit\mathbf{E} \end{pmatrix} = \begin{pmatrix} \mathbf{E}_0 \\ \mathbf{H}_0 \\ \diamondsuit\mathbf{E}_0 \end{pmatrix}$$
$$+ \begin{pmatrix} a_1\bar{\mathbf{G}}_E \cdot \mathbf{p} + a_2\nabla \times \bar{\mathbf{G}}_H \cdot \mathbf{m} + a_3(\diamondsuit'\bar{\mathbf{G}}_E^T)^T \cdot \mathbf{Q} \\ \dfrac{a_1}{i\omega\mu\mu_0}\nabla \times \bar{\mathbf{G}}_E \cdot \mathbf{p} + a_4\bar{\mathbf{G}}_H \cdot \mathbf{m} + \dfrac{a_3}{i\omega\mu\mu_0}\nabla \times (\diamondsuit'\bar{\mathbf{G}}_E^T)^T \cdot \mathbf{Q} \\ a_1\diamondsuit\bar{\mathbf{G}}_E \cdot \mathbf{p} + a_2\diamondsuit(\nabla \times \bar{\mathbf{G}}_H) \cdot \mathbf{m} + a_3\diamondsuit(\diamondsuit'\bar{\mathbf{G}}_E^T)^T \cdot \mathbf{Q} \end{pmatrix} \qquad (8)$$

where in the SI unit system $a_1 = \omega^2\mu\mu_0$, $a_2 = i\omega$, $a_3 = a_1/6$, $a_4 = \omega^2\varepsilon\varepsilon_0$. This result combines the magnetoelectric Green dyadic[31] with the electric field radiated by a quadrupole[56,57] $\mathbf{Q}$ that is given by $\mathbf{E}(\mathbf{r}) = (1/6)\omega^2\mu_0\mu\ (\diamondsuit'\bar{\mathbf{G}}_E^T(\mathbf{r},\mathbf{r}'))^T\cdot\mathbf{Q}$. Equation 7 is of the form $\mathcal{P} = \bar{\alpha}^S[\mathcal{E}_0 + \mathcal{GP}]$, where $\mathcal{P}$ is the generalized induced moment, $\mathcal{E}_0$ is the driving field, and $\mathcal{G}$ is a generalized field propagator that includes the Green's function and the curl of the Green's function, as well as its symmetric

gradients. Hence, the corrected polarizability defined through $\mathcal{P} = \bar{\alpha}^S_{\text{corrected}} \mathcal{E}_0$ must be expressed in the commonly used form $\bar{\alpha}^S_{\text{corrected}}{}^{-1} = \bar{\alpha}^{S^{-1}} - \mathcal{G}$. Explicitly, we define the corrected $\bar{\alpha}^S_{\text{corrected}}$ tensor as

$$
\bar{\alpha}^S_{\text{corrected}}{}^{-1} = \bar{\alpha}^{S^{-1}} - ...
$$

$$
\begin{pmatrix}
a_1 \bar{\mathbf{G}}_E & a_2 \nabla \times \bar{\mathbf{G}}_H & a_3(\hat{\diamondsuit}' \bar{\mathbf{G}}_E^T)^T \\
\dfrac{a1}{i\omega\mu\mu_0} \nabla \times \bar{\mathbf{G}}_E & a_4 \bar{\mathbf{G}}_H & \dfrac{a_3}{i\omega\mu\mu_0} \nabla \\
 & & \times (\hat{\diamondsuit}' \bar{\mathbf{G}}_E^T)^T \\
a_1 \hat{\diamondsuit} \bar{\mathbf{G}}_E & a_2 \hat{\diamondsuit}(\nabla \times \bar{\mathbf{G}}_H) & a_3 \hat{\diamondsuit}(\hat{\diamondsuit}' \bar{\mathbf{G}}_E^T)^T
\end{pmatrix}
$$

$$(9)$$

where the actual inversion again requires casting to and from 11 × 11 form as outlined in the Methods. In absence of quadrupolar contributions, this correction reduces to the magnetoelectric radiation damping correction derived for metamaterials by Belov[58] and Sersic,[31] which in itself is a generalization of the Sipe-Kranendonk formalism.[59] Note that owing to the required matrix inversion, a nontrivial environment such as a nearby surface can *induce* magnetoelectric cross-coupling,[60] as well as mixing of dipolar and quadrupolar excitations.

## ■ SINGLE PARTICLE ON A SI SUBSTRATE AS DIRECTIONAL ANTENNA

We apply the correction to the superpolarizability tensor of Au disks fabricated on a Si substrate which were recently used in a simple cathodoluminescence experiment.[61] We take a pillbox as particle shape with a diameter of 180 nm and a height of 80 nm. We retrieve the superpolarizability for the particle in vacuum, and subsequently correct with the backaction correction (evaluated at midheight, i.e., 40 nm above the silicon substrate).

Figure 5b,c summarizes $\alpha^S$ as color plots before and after the correction, taking as wavelength 565 nm and again scaling the superpolarizability tensor elements (Methods) such that equal value means equal scattered power. We present a logarithmic color plot to facilitate quick identification of relevant entries (Supporting Information provides numerical values). In the absence of the substrate, the particle response is dominated by a strong electric polarizability along the three principal particle axes. Here $x$ and $y$ are strictly degenerate by symmetry, while the polarizability along $z$ is somewhat lower with a ratio of 0.34 owing to the smaller height. The isolated disk also allows a significant magnetic dipole response and quadrupolar response owing to the big disk size. The particle symmetry, however, implies absence of bianisotropy. Once the disk is brought close to the substrate, the substrate induces cross-coupling between different elements, namely, bianisotropy linking electric and magnetic dipoles ($p_x$ and $m_y$) and coupling of dipolar and quadrupolar responses.

To gain more insight we highlight the polarizability tensor elements that are relevant in a typical normal incidence scattering experiment, that is, when impinging with an "$x$" polarized plane wave. The most important elements in the superpolarizability tensor that play a role, that is, $\alpha^{E_x}_{p_x}$, $\alpha^{E_x}_{m_y}$, $\alpha^{H_y}_{m_y}$, and $\alpha^{E_x}_{Q_{xz}}$ are plotted as a function of wavelength in Figure 5d. For the particle in free space, the strongest contribution to the scattering is simply the purely electric dipolar response $\alpha^{E_x}_{p_x}$, with a maximum of $1.8 \times 10^{-2}$ $\mu m^3$ at a wavelength of 680 nm. The
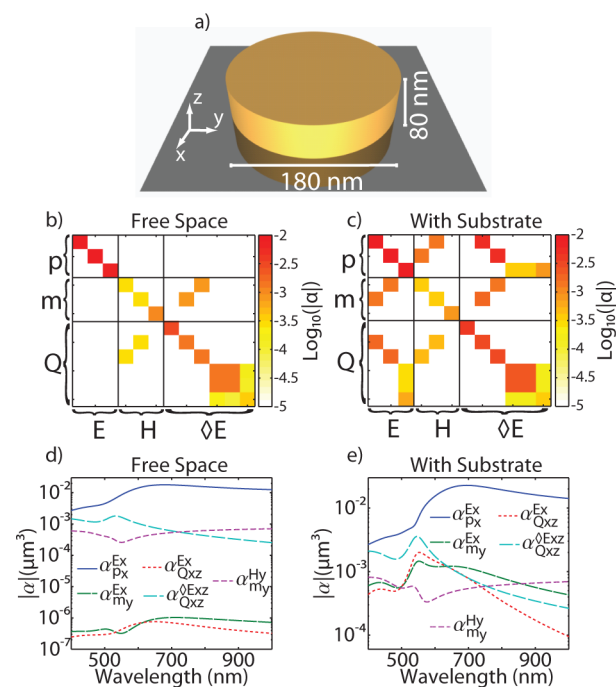


**Figure 5.** (a) Sketch of a gold disk on silicon. (b, c) Graphical representation of the superpolarizability tensor at $\lambda = 565$ nm of an isolated disk (b) and the same disk on silicon (d). As in Figure 3 the color scale represents $\log_{10}(|\alpha^S|)$, where $\alpha^S$ is expressed in $\mu m^3$. (d, e) Wavelength dependence of salient superpolarizability components for the isolated disk (d), and the disk on the Si substrate (e).

next-important terms, that is, the magnetic dipole response $\alpha^{H_y}_{m_y}$ and electric quadrupole $\alpha^{\diamondsuit E_{xz}}_{Q_{xz}}$ are 10 to 100 times smaller, while the off-diagonal cross polarizability is another factor of 100 to 1000 smaller still.

Once the scatterer is placed on the substrate, the back action correction modifies this ordering. Figure 5e reveals that the electric polarizability is enhanced and shifted in frequency due to its interaction with the silicon substrate. Remarkably, the crosspolarizability $\alpha^{E_x}_{m_y}$ and hyperpolarizability $\alpha^{E_x}_{Q_{xz}}$ are enhanced by 3 to 4 orders of magnitude, thus allowing electric fields to much more efficiently excite magnetic dipoles and quadrupoles. An intuitive picture for this process is that if initially an electric dipole is induced in the scatterer, its image dipole has sufficient gradient for driving quadrupoles and the magnetic dipole.

On basis of recent experiments and theoretical proposals, it is expected that if one actually manages to excite magnetic dipole moments and electric quadrupoles as strongly as the fundamental electric dipole term, one can engineer complicated and directional radiation patterns.[53,62−64] Here we predict that if the Au antenna on silicon that we analyzed is excited with a localized source, as in cathodoluminescence, strongly directional radiation patterns indeed emerge. We predict these radiation patterns simply from two ingredients: the free-space superpolarizability and the known interface Green's function,[65] without any recourse to a full-wave solution beyond extraction of the superpolarizability of the disk in free space. To obtain a prediction we simply take as driving field (i.e., $\mathbf{E},\mathbf{H}$ and $\diamondsuit \mathbf{E}$) the field of an electric dipole emitter as given by the known interface Green function. Next, we calculate the induced moments by multiplication of the driving field with the substrate-corrected superpolarizability tensor. Finally we find the far-field radiation pattern by coherent addition of the

known far fields of the induced moments, for which asymptotic expansions are likewise textbook material.[65]

In Figure 6a we show the total field intensity squared ($|E|^2$) for the cylindrical Au antenna excited with a dipolar emitter
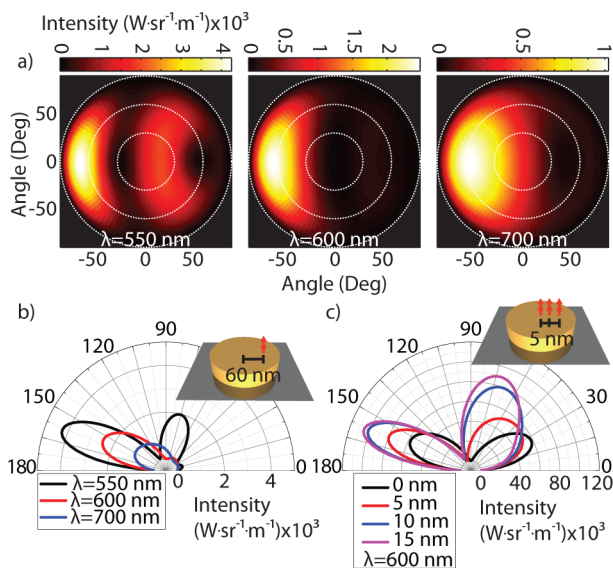


**Figure 6.** (a) Four field emission patterns for a gold cylinder antenna excited with a dipolar emitter located 40 nm above the point dipole—quadrupole and 60 nm off axis. The three graphs present different wavelengths 550, 600, and 700 nm. The white dashed circles display the angles 30, 60, and 90°. (b) Cross cuts of the $|E|^2$ emission patterns of (a). (c) Polar plots of the radiated intensity by the cylindrical antennas when excited with a electrical dipolar emitter located at different positions from the center of the antenna.

with strength $p_0$, located 60 nm off axis from the center of the cylinder and 40 nm above the center of the multipolar scatterer antenna. Figure 6a shows results for three driving wavelengths, namely, 550, 600, and 700 nm, which are the resonant wavelengths of the quadrupoles, in-plane electric dipole, and out of plane electric dipole, respectively. These figures together with the cross-cuts shown in Figure 6b show how we can achieve a very strong directional emission with only one single particle. The strong directionality results from coherent superposition of the electric dipole, magnetic dipole, and electric quadrupole terms that are excited in such a ratio as to yield comparable far-field flux. For instance, in the first panel of Figure 6a the antenna acquires an electric dipole of $|p_x| = 1.69p_0$, $|p_z| = 1.56p_0$ and a magnetic dipole of $|m_y| = 1.17p_0$, while the dominating acquired quadrupoles have a magnitude of $|Q_{xx}| = 3.86p_0$, $|Q_{yy}| = 3.61p_0$, and $|Q_{xz}| = 2.09p_0$.

Finally, we sweep the position of the dipole over the antenna, starting from the center moving in steps of only 5 nm. We find (Figure 6c) that the angular emission changes drastically with the position of the emitter with respect to the antenna. For instance, viewing emission under a 70° angle relative to the substrate, it is possible to acquire a signal that changes up to 15% between two given points per nm of lateral position shift of the excitation source. This effect could allow using simple gold antennas on a substrate as sensitive position detectors of fluorescent molecules with resolutions better than those of STORM[66] and PALM[67] microscopy. This ultrahigh sensitivity to position of a source relative to an antenna is similar in concept to a recent proposal to use a notched high-index dielectric sphere with an overlapping electric and magnetic

resonance.[63] However, practically fabricating an Au cylinder on a Si substrate is far simpler than preparing notched high-index Mie spheres.

## CONCLUSIONS

To summarize our work, we have presented a straightforward method to retrieve dipolar but also quadrupolar polarizabilities $\alpha^Q$ for arbitrary scatterers in order to provide substantiation for hybridization intuition, and input for quantitative hybridization reasoning for plasmonic antenna structures. A key simplification is to handle quadrupolar terms through the $\diamondsuit$ operator to avoid redundancy and ease visualization. As an example we have analyzed the plasmonic dolmen structure, providing a quantitative underpinning for reported hybridization intuition in terms of electric dipole-to-quadrupole coupling. In addition to quantifying the strength of the induced moments, the retrieval also evidenced a commonly disregarded but equally important magnetic dipole moment. This example clearly shows very large potential of superpolarizability retrieval for the quantitative understanding of many complex plasmon and dielectric antenna phenomena. In addition we have shown how to predict the scattering properties of a building block in a complex environment on the basis of on one hand the free space building block polarizability and on the other hand the environment Green function. This will have a large impact on the quantitative modeling of plasmon and dielectric antennas in typical applications for solar cells, LEDs, and sensors, where antennas always function in a complicated dielectric environment. Importantly, the complex environment can induce or enhance particular multipolar moments, yielding new methods to control directionality of scattering and emission.

## METHODS

**Units.** In order to be able to compare the magnitudes of driving field components, polarizabilities, and induced moments directly, we use a non-SI scaling of quantities based on the CGS unit system. Here we provide the unit conversion to SI. The rationale is that equal entries in the polarizability tensor correspond to equal scattered power.

First we scale the electric field, magnetic field, and electric field gradient to share as common unit [V/m], scaled such that a simple plane wave represents unit strength for all its nonzero components. The conversion reads

$$\mathbf{E} = \mathbf{E}_{SI}, \quad \mathbf{H} = Z_0\mathbf{H}_{SI}, \quad \text{and} \quad \diamondsuit\mathbf{E} = k\diamondsuit\mathbf{E}_{SI} \qquad (10)$$

where $Z_0$ is the free space impedance. Next we scale all the induced moments from their SI definition so as to obtain as common unit [C m] (Coulomb meter) and such that any moment of unit strength radiates exactly the same power into the far-field. The conversion reads

$$\mathbf{p} = \mathbf{p}_{SI}, \quad \mathbf{m} = 1/c\,\mathbf{m}_{SI}, \quad \text{and} \quad \mathbf{Q} = \frac{k}{\sqrt{60}}\mathbf{Q}_{SI} \qquad (11)$$

The factor $k/\sqrt{60}$ results from the quadrupolar equivalent of Larmor's formula. For a dipole, Larmor's formula states that the radiated power is $P = c^2Z_0k^4/(12\pi)|\mathbf{p}_{SI}|^2$, while for a quadrupole $P = c^2Z_0k^6/(1440\pi)\sum_{\alpha,\beta}|Q_{SI,\alpha\beta}|^2$. Finally, with this choice of units the superpolarizability tensor is automatically cast to have units $\varepsilon_0 m^3$ for all entries, where comparable entries necessarily contribute comparably to the scattered power. We tabulate the complete conversion. For the block diagonals the conversion reads:

$$\alpha_{\mathbf{p}}^{\mathbf{E}} = \alpha_{\mathrm{SI}_{\mathbf{p}}}^{\mathbf{E}}, \quad \alpha_{\mathbf{m}}^{\mathbf{H}} = \frac{1}{Z_0 c}\alpha_{\mathrm{SI}_{\mathbf{m}}}^{\mathbf{H}}, \quad \text{and} \quad \alpha_{\mathbf{Q}}^{\lozenge\mathbf{E}} = \frac{k^2}{\sqrt{60}}\alpha_{\mathrm{SI}_{\mathbf{Q}}}^{\lozenge\mathbf{E}}$$

(12)

For the off-diagonal blocks, the conversion reads

$$\alpha_{\mathbf{m}}^{\mathbf{E}} = \frac{1}{c}\alpha_{\mathrm{SI}_{\mathbf{m}}}^{\mathbf{E}}, \quad \alpha_{\mathbf{p}}^{\mathbf{H}} = \frac{1}{Z_0}\alpha_{\mathrm{SI}_{\mathbf{p}}}^{\mathbf{H}}, \quad \alpha_{\mathbf{Q}}^{\mathbf{E}} = \frac{k}{\sqrt{60}}\alpha_{\mathrm{SI}_{\mathbf{Q}}}^{\mathbf{E}}$$

$$\alpha_{\mathbf{Q}}^{\mathbf{H}} = \frac{k}{Z_0\sqrt{60}}\alpha_{\mathrm{SI}_{\mathbf{Q}}}^{\mathbf{H}}, \quad \alpha_{\mathbf{p}}^{\lozenge\mathbf{E}} = k\alpha_{\mathrm{SI}_{\mathbf{p}}}^{\lozenge\mathbf{E}}, \quad \alpha_{\mathbf{m}}^{\lozenge\mathbf{E}} = \frac{k}{c}\alpha_{\mathrm{SI}_{\mathbf{p}}}^{\lozenge\mathbf{E}}$$

(13)

Due to our definition of the vector $\mathbf{Q}$, the rows 7, 8, and 9 in $\alpha^S$ are divided by 2. In Figures 3 and 5 we further take out the factor $\varepsilon_0$ so that the plotted quantity has units of volume and can be directly compared to particle volume.

**Casting 12 × 12 $\alpha^S$ to Nonredundant Subspace and Back.** That the quadrupole tensor is traceless $Q_{xx} + Q_{yy} + Q_{zz} = 0$, and $\mathbf{E}$ is divergence free, that is, $\partial_x E_x + \partial_y E_y + \partial_z E_z = 0$ implies that the 12 × 12 superpolarizability tensor is not invertible, as it has a matrix rank 11. The redundancy can be removed by replacing $\mathbf{Q}$ by $\hat{\mathbf{Q}} = \{2Q_{xy}, 2Q_{xz}, 2Q_{yz}, Q_{xx}, Q_{yy}\}$ and $\lozenge\mathbf{E}$ by $\hat{\lozenge}\mathbf{E} = \{(\partial_x E_y + \partial_y E_x)/2, (\partial_x E_z + \partial_z E_x)/2, (\partial_y E_z + \partial_z E_y)/2, (\partial_x E_x - \partial_z\partial E_z), (\partial_y E_y - \partial_z E_z)\}$. To cast the 12 × 12 tensor $\alpha^S$ in 11 × 11 form $\hat{\alpha}^S$ requires simply dropping the last column and row. Procedurally we first find the 11 × 11 $\hat{\alpha}^S$ tensor from the moments $(\mathbf{p}, \mathbf{m}, \hat{\mathbf{Q}})$ induced by 11 incidence conditions, and then expand to 12 × 12 form. To this end we define the 11 × 12 matrix $M$, which has the 11 × 11 identity matrix as upper diagonal block, and which as last column has zeros except for its last two entries $M_{11,11} = M_{11,12} = -1$. With this definition, the expanded polarizability is retrieved as $\alpha^S = M^T\hat{\alpha}^S M$. The backaction correction in eq 9 is implemented by taking the uncorrected 11 × 11 superpolarizability $\hat{\alpha}^S$, calculating the Green function term replacing $\lozenge$ by $\hat{\lozenge}$ and, finally, casting the corrected $\hat{\alpha}^S$ to 12 × 12 form. We note that casting into 12 × 12 form is not strictly necessary since the 11 × 11 form contains all information. However, the 12 × 12 form is easier to interpret.

## ■ ASSOCIATED CONTENT

**ⓢ Supporting Information**

Quantitative values for all non-negligible tensor elements and additional details as stated in the text. This material is available free of charge via the Internet at http://pubs.acs.org.

## ■ AUTHOR INFORMATION

**Corresponding Author**

*E-mail: f.koenderink@amolf.nl.

**Notes**

The authors declare no competing financial interest.

## ■ ACKNOWLEDGMENTS

## ■ REFERENCES

(1) Novotny, L.; van Hulst, N. Antennas for Light. *Nat. Photonics* **2011**, *5*, 83−90.

(2) Schuller, J. A.; Barnard, E. S.; Cai, W.; Jun, Y. C.; White, J. S.; Brongersma, M. L. Plasmonics for Extreme Light Concentration and Manipulation. *Nat. Mater.* **2010**, *9*, 193−204.

(3) Agio, M., Alú, A., Eds. *Optical Antennas*; Cambridge University Press: New York, 2013.

(4) Pillai, S.; Catchpole, K. R.; Trupke, T.; Green, M. A. Surface Plasmon Enhanced Silicon Solar Cells. *J. Appl. Phys.* **2007**, *101*, 093105.

(5) Atwater, H. A.; Polman, A. Plasmonics for Improved Photovoltaic Devices. *Nat. Mater.* **2010**, *9*, 205−213.

(6) Lozano, G.; Louwers, D. J.; Rodriguez, S. R. K.; Murai, S.; Jansen, O. T.; Verschuuren, M. A.; Gómez Rivas, J. Plasmonics for Solid-State Lighting: Enhanced Excitation and Directional Emission of Highly Efficient Light Sources. *Light Sci. Appl.* **2013**, *2*, e66.

(7) Giannini, V.; Fernández-Domnguez, A. I.; Heck, S. C.; Maier, S. A. Plasmonic Nanoantennas: Fundamentals and Their Use in Controlling the Radiative Properties of Nanoemitters. *Chem. Rev.* **2011**, *111*, 3888−3912.

(8) Anger, P.; Bharadwaj, P.; Novotny, L. Enhancement and Quenching of Single-Molecule Fluorescence. *Phys. Rev. Lett.* **2006**, *96*, 113002.

(9) Kühn, S.; Håkanson, U.; Rogobete, L.; Sandoghdar, V. Enhancement of Single-Molecule Fluorescence Using a Gold Nanoparticle as an Optical Nanoantenna. *Phys. Rev. Lett.* **2006**, *97*, 017402.

(10) Koenderink, A. F. Plasmon Nanoparticle Array Waveguides for Single Photon and Single Plasmon Sources. *Nano Lett.* **2009**, *9*, 4228−4233.

(11) Curto, A. G.; Volpe, G.; Taminiau, T. H.; Kreuzer, M. P.; Quidant, R.; van Hulst, N. F. Unidirectional Emission of a Quantum Dot Coupled to a Nanoantenna. *Science* **2010**, *329*, 930−933.

(12) Kinkhabwala, A.; Yu, Z.; Fan, S.; Avlasevich, Y.; Mullen, K.; E, M. Large Single-Molecule Fluorescence Enhancements Produced by a Bowtie Nanoantenna. *Nat. Photonics* **2009**, *3*, 654−657.

(13) Punj, D.; Mivelle, M.; Moparthi, S. B.; van Zanten, T. S.; Rigneault, H.; van Hulst, N. F.; Garcia-Parajo, M. F.; Wenger, J. A Plasmonic "Antenna-in-Box" Platform for Enhanced Single-Molecule Analysis at Micromolar Concentrations. *Nat. Nanotechnol.* **2013**, *8*, 512−516.

(14) Anker, J. N.; Hall, W. P.; Lyandres, O.; Shah, N. C.; Zhao, J.; Van Duyne, R. P. Biosensing with Plasmonic Nanosensors. *Nat. Mater.* **2008**, *7*, 442−453.

(15) Escobedo, C.; Brolo, A. G.; Gordon, R.; Sinton, D. Optofluidic Concentration: Plasmonic Nanostructure as Concentrator and Sensor. *Nano Lett.* **2012**, *12*, 1592−1596.

(16) Ferreira, J.; Santos, M. J. L.; Rahman, M. M.; Brolo, A. G.; Gordon, R.; Sinton, D.; Girotto, E. M. Attomolar Protein Detection Using In-Hole Surface Plasmon Resonance. *J. Am. Chem. Soc.* **2009**, *131*, 436−437.

(17) Yu, N.; Genevet, P.; Kats, M. A.; Aieta, F.; Tetienne, J.-P.; Capasso, F.; Gaburro, Z. Light Propagation with Phase Discontinuities: Generalized Laws of Reflection and Refraction. *Science* **2011**, *334*, 333−337.

(18) Ni, X.; Emani, N. K.; Kildishev, A. V.; Boltasseva, A.; Shalaev, V. M. Broadband Light Bending with Plasmonic Nanoantennas. *Science* **2012**, *335*, 427.

(19) Prodan, E.; Radloff, C.; Halas, N. J.; Nordlander, P. A Hybridization Model for the Plasmon Response of Complex Nanostructures. *Science* **2003**, *302*, 419−422.

(20) Weber, W. H.; Ford, G. W. Propagation of Optical Excitations by Dipolar Interactions in Metal Nanoparticle Chains. *Phys. Rev. B* **2004**, *70*, 125429.

(21) García de Abajo, F. J. Colloquium: Light Scattering by Particle and Hole Arrays. *Rev. Mod. Phys.* **2007**, *79*, 1267−1290.

(22) Bernal Arango, F.; Kwadrin, A.; Koenderink, A. F. Plasmonic Antennas Hybridized with Dielectric Waveguides. *ACS Nano* **2012**, *6*, 10156−10167.

(23) Lukyanchuk, B.; Zheludev, N. I.; Maier, S. A.; Halas, N. J.; Nordlander, P.; Giessen, H.; Chong, C. T. The Fano Resonance in Plasmonic Nanostructures and Metamaterials. *Nat. Mater.* **2010**, *9*, 707−715.

(24) Liu, N.; Langguth, L.; Weiss, T.; Kastel, J.; Fleischhauer, M.; Pfau, T.; Giessen, H. Plasmonic Analogue of Electromagnetically Induced Transparency at the Drude Damping Limit. *Nat. Mater.* **2009**, *8*, 758−762.

(25) Hao, F.; Sonnefraud, Y.; Dorpe, P. V.; Maier, S. A.; Halas, N. J.; Nordlander, P. Symmetry Breaking in Plasmonic Nanocavities: Subradiant LSPR Sensing and a Tunable Fano Resonance. *Nano Lett.* **2008**, *8*, 3983−3988.

(26) Verellen, N.; Sonnefraud, Y.; Sobhani, H.; Hao, F.; Moshchalkov, V. V.; Dorpe, P. V.; Nordlander, P.; Maier, S. A. Fano Resonances in Individual Coherent Plasmonic Nanocavities. *Nano Lett.* **2009**, *9*, 1663−1667.

(27) Mirin, N. A.; Bao, K.; Nordlander, P. Fano Resonances in Plasmonic Nanoparticle Aggregates. *J. Phys. Chem. A* **2009**, *113*, 4028−4034.

(28) Frimmer, M.; Coenen, T.; Koenderink, A. F. Signature of a Fano Resonance in a Plasmonic Metamolecule's Local Density of Optical States. *Phys. Rev. Lett.* **2012**, *108*, 077404.

(29) Park, S. Y.; Stroud, D. Surface-Plasmon Dispersion Relations in Chains of Metallic Nanoparticles: An Exact Quasistatic Calculation. *Phys. Rev. B* **2004**, *69*, 125418.

(30) Gallinet, B.; Martin, O. J. F. Relation between Near-Field and Far-Field Properties of Plasmonic Fano Resonances. *Opt. Express* **2011**, *19*, 22167−22175.

(31) Sersic, I.; Tuambilangana, C.; Kampfrath, T.; Koenderink, A. F. Magnetoelectric Point Scattering Theory for Metamaterial Scatterers. *Phys. Rev. B* **2011**, *83*, 245102.

(32) Jackson, J. D. *Classical Electrodynamics*, 3rd ed.; Wiley: New York, 1999.

(33) Mühlig, S.; Menzel, C.; Rockstuhl, C.; Lederer, F. Multipole Analysis of Meta-Atoms. *Metamaterials* **2011**, *5*, 64−73.

(34) Kern, A. M.; Martin, O. J. F. Surface Integral Formulation for 3D Simulations of Plasmonic and High Permittivity Nanostructures. *J. Opt. Soc. Am. A* **2009**, *26*, 732−740.

(35) Bernal Arango, F.; Koenderink, A. F. Polarizability Tensor Retrieval for Magnetic and Plasmonic Antenna Design. *New. J. Phys.* **2013**, *15*, 073023.

(36) Tai, C. T. *Dyadic Green's Functions in Electromagnetic Theory*, 2nd ed.; IEEE Press: New York, 1993.

(37) Mohlenkamp, M. J. A Fast Transform for Spherical Harmonics. *J. Fourier Anal. Appl.* **1999**, *5*, 159−184.

(38) Satten, R. A. Effects of Atomic Quadrupole Moments upon the Index of Refraction. *J. Chem. Phys.* **1957**, *26*, 766−772.

(39) Alù, A.; Engheta, N. Guided Propagation along Quadrupolar Chains of Plasmonic Nanoparticles. *Phys. Rev. B* **2009**, *79*, 235412.

(40) Evlyukhin, A. B.; Reinhardt, C.; Zywietz, U.; Chichkov, B. N. Collective Resonances in Metal Nanoparticle Arrays with Dipole-Quadrupole Interactions. *Phys. Rev. B* **2012**, *85*, 245411.

(41) Zhang, S.; Genov, D. A.; Wang, Y.; Liu, M.; Zhang, X. Plasmon-Induced Transparency in Metamaterials. *Phys. Rev. Lett.* **2008**, *101*, 047401.

(42) Liu, N.; Weiss, T.; Mesch, M.; Langguth, L.; Eigenthaler, U.; Hirscher, M.; Sonnichsen, C.; Giessen, H. Planar Metamaterial Analogue of Electromagnetically Induced Transparency for Plasmonic Sensing. *Nano Lett.* **2010**, *10*, 1103−1107.

(43) Liu, N.; Hentschel, M.; Weiss, T.; Alivisatos, A. P.; Giessen, H. Three-Dimensional Plasmon Rulers. *Science* **2011**, *332*, 1407−1410.

(44) Ye, Z.; Zhang, S.; Wang, Y.; Park, Y.-S.; Zentgraf, T.; Bartal, G.; Yin, X.; Zhang, X. Mapping the Near-Field Dynamics in Plasmon-Induced Transparency. *Phys. Rev. B* **2012**, *86*, 155148.

(45) Palik, E. D. *Handbook of Optical Constants of Solids*; Academic Press: Boston, 1985.

(46) Serdyukov, A.; Semchenko, I.; Tretyakov, S.; Sihvola, A. In *Electromagnetics of Bi-anisotropic Materials: Theory and Applications*, 1st ed.; de Cogan, D., Ed.; Electrocomponent Science Monographs; Gordon and Breach Science: Amsterdam, The Netherlands, 2001.

(47) Dolling, G.; Enkrich, C.; Wegener, M.; Zhou, J. F.; Soukoulis, C. M.; Linden, S. Cut-Wire Pairs and Plate Pairs as Magnetic Atoms for Optical Metamaterials. *Opt. Lett.* **2005**, *30*, 3198−3200.

(48) Lam, V. D.; Kim, J. B.; Lee, S. J.; Lee, Y. P.; Rhee, J. Y. Dependence of the Magnetic-Resonance Frequency on the Cut-Wire Width Offcut-Wire Pair Medium. *Opt. Express* **2007**, *15*, 16651−16656.

(49) Meyrath, T. P.; Zentgraf, T.; Rockstuhl, C.; Giessen, H. Electromagnetic Induction in Metamaterials. *Appl. Phys. B: Laser Opt.* **2008**, *93*, 107−110.

(50) Taminiau, T. H.; Karaveli, S.; van Hulst, N. F.; Zia, R. Quantifying the Magnetic Nature of Light Emission. *Nat. Commun.* **2012**, *3*, 979.

(51) Koenderink, A. F.; Polman, A. Complex Response and Polariton-Like Dispersion Splitting in Periodic Metal Nanoparticle Chains. *Phys. Rev. B* **2006**, *74*, 033402.

(52) Zheng, X.; Volskiy, V.; Valev, V.; Vandenbosch, G.; Moshchalkov, V. Line Position and Quality Factor of Plasmonic Resonances Beyond the Quasi-Static Limit: A Full-Wave Eigenmode Analysis Route. *J. Sel. Top. Quant. Electron.* **2013**, *19*, 4600908−4600908.

(53) Curto, A. G.; Taminiau, T. H.; Volpe, G.; Kreuzer, M. P.; Quidant, R.; van Hulst, N. F. Multipolar Radiation of Quantum Emitters with Nanowire Optical Antennas. *Nat. Commun.* **2013**, *4*, 1750:1−7.

(54) Buchler, B. C.; Kalkbrenner, T.; Hettich, C.; Sandoghdar, V. Measuring the Quantum Efficiency of the Optical Emission of Single Radiating Dipoles Using a Scanning Mirror. *Phys. Rev. Lett.* **2005**, *95*, 063003.

(55) Frimmer, M.; Koenderink, A. F. Superemitters in Hybrid Photonic Systems: A Simple Lumping Rule for the Local Density of Optical States and Its Breakdown at the Unitary Limit. *Phys. Rev. B* **2012**, *86*, 235428.

(56) Klimov, V. V.; Ducloy, M. Quadrupole Transitions Near an Interface: General Theory and Application to an Atom inside a Planar Cavity. *Phys. Rev. A* **2005**, *72*, 043809.

(57) Ribaric, M.; Sustersic, L. Expansion in Terms of Moments of Time-Dependent, Moving Charges and Currents. *SIAM J. Appl. Math.* **1995**, *55*, 593−624.

(58) Belov, A.; Maslovski, S. I.; Simovski, K. R.; Tretyakov, S. A. A Condition Imposed on the Electromagnetic Polarizability of a Bianisotropic Lossless Scatterer. *Technol. Phys. Lett.* **2003**, *29*, 718−720.

(59) Sipe, J. E.; Kranendonk, J. V. Macroscopic Electromagnetic Theory of Resonant Dielectrics. *Phys. Rev. A* **1974**, *9*, 1806−1822.

(60) Kwadrin, A.; Koenderink, A. F. Probing the Electrodynamic Local Density of States with Magneto-Electric Point Scatterers. *Phys. Rev. B* **2013**, *86*, 125123.

(61) Coenen, T.; Bernal Arango, F.; Koenderink, A. F.; Polman, A. Nanoscale Excitation and Emission Control of Individual Plasmonic Scatterers. *Nat. Commun.* **2014**, *5*, 3250 DOI: 10.1038/ncomms4250.

(62) Rolly, B.; Stout, B.; Bonod, N. Boosting the directivity of optical antennas with magnetic and electric dipolar resonant particles. *Opt. Express* **2012**, *20*, 20376−20386.

(63) Krasnok, A.; Filonov, D.; Slobozhanyuk, A.; Simovski, C.; Belov, P.; Kivshar, Y. Superdirective Dielectric Nanoantennas with Effect of Light Steering. *arXiv* **2013** *1307.4601v1*, 8.

(64) Hancu, I. M.; Curto, A. G.; Castro-López, M.; Kuttge, M.; van Hulst, N. F. Multipolar Interference for Directed Light Emission. *Nano Lett.* **2014**, *14*, 166−171.

(65) Novotny, L.; Hecht, B. *Principles of Nano-Optics*; Cambridge University Press: Cambridge, 2006.

(66) Rust, M. J.; Bates, M.; Zhuang, X. Sub-Diffraction-Limit Imaging by Stochastic Optical Reconstruction Microscopy (STORM). *Nat. Methods* **2006**, *3*, 793−796.

(67) Betzig, E.; Patterson, G. H.; Sougrat, R.; Lindwasser, O. W.; Olenych, S.; Bonifacino, J. S.; Davidson, M. W.; Lippincott-Schwartz,

J.; Hess, H. F. Imaging Intracellular Fluorescent Proteins at Nanometer Resolution. *Science* **2006**, *313*, 1642−1645.